



Statistical Analysis of Torus and Kink Instabilities in Solar Eruptions

Ju Jing¹ , Chang Liu¹, Jeongwoo Lee^{1,2}, Hantao Ji³ , Nian Liu¹, Yan Xu¹, and Haimin Wang¹ 

¹Center for Solar-Terrestrial Research, New Jersey Institute of Technology, Newark, NJ 07102-1982, USA; ju.jing@njit.edu

²School of Space Research, Kyung Hee University, Yongin 17104, Republic of Korea

³Princeton Plasma Physics Laboratory, Princeton, NJ 08543, USA

Received 2018 June 18; revised 2018 July 27; accepted 2018 July 28; published 2018 September 10

Abstract

A recent laboratory experiment of ideal magnetohydrodynamic instabilities revealed four distinct eruption regimes readily distinguished by the torus instability (TI) and helical kink instability (KI) parameters. To establish its observational counterpart, we collected 38 solar flares (stronger than *GOES*-class M5 in general) that took place within 45° of disk center during 2011–2017, 26 of which are associated with a halo or partial halo coronal mass ejection (CME; i.e., ejective events), while the others are CME-less (i.e., confined events). This is a complete sample of solar events satisfying our selection criteria detailed in the paper. For each event, we calculate a decay index n of the potential strapping field above the magnetic flux rope (MFR) in and around the flaring magnetic polarity inversion line (a TI parameter) and the unsigned twist number T_w of the nonlinear force-free field lines forming the same MFR (a KI parameter). We then construct an n – T_w diagram to investigate how the eruptiveness depends on these parameters. We find that (1) T_w appears to play little role in discriminating between confined and ejective events; (2) the events with $n \gtrsim 0.8$ are all ejective, and all confined events have $n \lesssim 0.8$. However, $n \gtrsim 0.8$ is not a necessary condition for eruption because some events with $n \lesssim 0.8$ also erupted. In addition, we investigate the MFR’s geometrical parameters, apex height, and distance between footpoints, as a possible factors for the eruptiveness. We briefly discuss the difference of the present result for solar eruptions with that of the laboratory result in terms of the role played by magnetic reconnection.

Key words: Sun: activity – Sun: coronal mass ejections (CMEs) – Sun: flares – Sun: magnetic fields

1. Introduction

A solar flare is primarily considered to be a low-atmosphere tracer of magnetic explosions/eruptions. In terms of outcome, there are two types of flares: ejective and confined (Moore et al. 2001). Ejective flares are accompanied by coronal mass ejections (CMEs), while confined flares do not have associated CMEs.

A magnetic flux rope (MFR), characterized by a twisted and writhed topological structure, is thought to be a fundamental structure underlying the phenomenon of CMEs. Although the initiation mechanisms are still under debate, it is now common to explain the onset conditions of an MFR eruption in the context of two ideal magnetohydrodynamic (MHD) instabilities, the torus instability (TI; Kliem & Török 2006) and helical kink instability (KI; Török et al. 2004). TI and KI are mainly controlled by the structural properties of the strapping magnetic field (i.e., the ambient field that runs perpendicular to the MFR) and the guide magnetic field (the ambient field that runs toroidally along the MFR), respectively. Simply put, TI occurs when the strapping field above the MFR declines with height at a sufficiently steep rate, as quantified by decay index n (Török & Kliem 2005, 2007; Kliem & Török 2006). The TI onset criterion of $n \geq n_{\text{crit}} = 1.5$ was first derived analytically by Bateman (1978) and some MHD simulations have found similar values (Kliem & Török 2006; Aulanier et al. 2010). A number of other analytical/numerical studies suggest that this critical index, n_{crit} , may lie in a wider range of $0.5 < n_{\text{crit}} < 2$ (Fan & Gibson 2007; Démoulin & Aulanier 2010; Fan 2010; Olmedo & Zhang 2010; Zuccarello et al. 2015). KI, on the other hand, occurs when an MFR is twisted by more than a critical value. The minimum critical twist Φ_{crit} found among analytical/numerical studies is 2.5π (corresponding to 1.25 field line windings about the rope axis; e.g., Hood & Priest 1981; Baty 2001; Török & Kliem 2003; Fan &

Gibson 2003). The slow decay of strapping field with height may help confine MFRs, and, in some simulation cases, allows MFRs to build up twist for developing KI (Fan & Gibson 2007).

Observationally, investigations on what magnetic factors determine the likelihood of ejective/confined eruptions have largely focused on one or two aspects: the decay index n of the potential strapping field (e.g., Liu 2008; Guo et al. 2010; Liu et al. 2010a; Nindos et al. 2012; Baumgartner et al. 2018), and/or the non-potentiality of active regions (ARs) such as free magnetic energy, relative magnetic helicity, magnetic twist, etc. (e.g., Nindos & Andrews 2004; Falconer et al. 2006, 2009; Tziotziou et al. 2012; Lee et al. 2016; Toriumi et al. 2017). It has been found in some well-studied cases that confined flares are often hosted by ARs with a stronger strapping field and weaker non-potentiality in comparison to ejective ones (Jing et al. 2015; Sun et al. 2015). For ejective events, the CME speed shows a positive correlation with the decay index of hosting ARs (Xu et al. 2012; Cui et al. 2018).

It is worth noting that an unprecedented laboratory experiment designed to study the Sun-like line-tied MFRs reveals four distinct eruption regimes that are readily distinguished by the TI and KI parameters (Myers et al. 2015, see their Figure 2). In the four regimes MFRs are either eruptive, stable, failed kink (i.e., torus-stable MFRs that exceed the kink threshold fail to erupt), or failed torus (i.e., kink-stable MFRs that exceed the torus threshold fail to erupt). Such an experimental result on the TI and KI has direct implications for eruptions in the solar corona, and its observational counterpart remains to be established, which is the motivation of this study. In this paper, we present the TI versus KI parameter diagram, established from a statistical study using solar observations together with the coronal field extrapolation techniques. The goal of this study is to improve

our understanding of the requirements for a solar eruption: what the trigger/driver mechanisms might be and what, if any, onset criteria must be reached.

2. Sample Selection and Methods

We examined NOAA *GOES* soft X-ray (SXR) flare reports to search for major flares (stronger than *GOES*-class M5 in general) that occurred within 45° of the disk center over a seven-year period from 2011 January to 2017 December. Due to the small sample size of confined flares, we relaxed the SXR class requirement from M5 to M4 for confined flares. To avoid the over-representation of a certain flare-productive AR, at most, two flares per AR were included in the samples: the one with the greatest SXR magnitude and the one nearest to the disk center.

For each flare, its CME association was determined by reference to the *LASCO* CME catalog (Gopalswamy et al. 2009). We regarded a flare as ejective if the following criteria were fulfilled: (1) the CME onset time at R_\odot extrapolated backward from the CME height–time profile reasonably agrees with the flare onset time; and (2) the position angle of the CME agrees with the quadrant on the Sun in which the flare occurred. When a flare–CME association is identified, we also refer to the *LASCO* CME catalog for the CME kinetic energy and use it as a CME parameter (Vourlidas et al. 2010). We then excluded those ejective flares from the samples if their associated CMEs are neither halo nor partial halo, because the other types (for example, a jet-type) of CMEs may not be compatible with an MFR topology. We regarded a flare as confined if there are no CMEs in temporal and spatial proximity as described above.

The sample selection requirements led us to a total of 38 flares (26 ejective and 12 confined) from 27 different ARs. Table 1 summarizes the properties of the flares and the CME kinetic energy E_{CME} (if ejective). The last five columns list free magnetic energy E_{free} (a measure of the non-potentiality of ARs), apex height h_{apex} and footpoint distance d of MFRs, decay index n of the strapping field (a TI parameter; see Section 3.1), and twist number T_w of the MFR (a KI parameter; see Section 3.2). The calculation of all these parameters involves coronal magnetic field measurements, which are hardly accessible from observations but can be reconstructed using a technique called coronal field extrapolation.

For each event, we used the last available vector magnetograms (`hmi.sharp_cea_720s`) of the AR prior to the flare, obtained by the the Helioseismic and Magnetic Imager (HMI; Schou et al. 2012) on board the *Solar Dynamics Observatory* (*SDO*), as the boundary conditions for the coronal field extrapolation. The magnetograms were re-mapped using a cylindrical equal area projection and presented as (B_r, B_θ, B_ϕ) in heliocentric spherical coordinates corresponding to (B_z, B_y, B_x) in heliographic coordinates (Sun 2013). We re-binned the magnetograms to $1''$ pixel intervals and pre-processed the data toward the force-free conditions (Wiegelmann et al. 2006). Then we performed the three-dimensional (3D) nonlinear force-free (NLFF) field and potential field extrapolations with the weighted optimization method (Wiegelmann 2004) and the method of Alissandrakis (1981), respectively. In particular, the weighted optimization method of Wiegelmann (2004) is an implementation of the original optimization algorithm of Wheatland et al. (2000) and has been optimized for the *SDO*/HMI magnetogram data (Wiegelmann et al. 2012). The x - and y -dimensions of the 3D computational domain V vary from case to case according to ARs’s size to cover not only the major portion of ARs but also the plage regions

surrounding the ARs, and the z -dimension of V is set to be $200''$ (~ 145 Mm) in all the cases.

To assess the performance of NLFF field extrapolations, for each event, we computed the $\langle \text{CWsin}\theta \rangle^4$ metric and the $\langle |f_i| \rangle^5$ metric (see De Rosa et al. 2009 for details). Briefly, $\langle \text{CWsin}\theta \rangle$ and $\langle |f_i| \rangle$ measure how well the force-free and divergence-free conditions are satisfied in the NLFF field models, with perfectly force-free and divergence-free fields having $\langle \text{CWsin}\theta \rangle = 0$ and $\langle |f_i| \rangle = 0$, respectively. The average of all values of $\langle \text{CWsin}\theta \rangle$ over our 38 samples is 0.13 ± 0.04 , and that of $\langle |f_i| \rangle$ is $(4.4 \pm 1.1) \times 10^{-4}$, suggesting a well-satisfied force-free and divergence-free condition.

Based on both NLFF and potential fields, we estimated free magnetic energy E_{free} over the 3D computational domain V as follows:

$$E_{\text{free}} = E_{\text{NLFF}} - E_p = \int \frac{B_{\text{NLFF}}^2}{8\pi} dV - \int \frac{B_p^2}{8\pi} dV, \quad (1)$$

where the superscripts NLFF and p represent the NLFF field and the potential field, respectively. E_{free} calculated in this way is regarded as the maximum energy available for powering flares/CMEs in a given AR. The uncertainty of E_{free} caused by the boundary conditions was previously evaluated by the code testing conducted by Wiegelmann & Inhester (2010), in which the same extrapolation code was applied to a well-known semi-analytic test case of Low & Lou (1990). It is found that, for example, for a relatively high noise level of 5% in the transverse field, the reconstructed NLFF field is able to reproduce the reference field with an underestimation of 12%–14% in E_{NLFF} (Wiegelmann & Inhester 2010), which may lead to an uncertainty of $\sim 39\%$ in E_{free} . The value of E_{free} calculated from our NLFF and potential fields with a 39% uncertainty is listed in Table 1.

The TI and KI parameters were inferred from the NLFF field model and potential field model, respectively, as described in the following section.

3. TI and KI Parameters

The estimation of TI and KI parameters is illustrated in Figures 1 and 2, using the ejective M6.5 (SOL2015-06-22T18:23) flare of AR 12371 and the confined M4.2 (SOL2015-03-12T14:08) flare of AR 12297 as examples, respectively.

3.1. TI Parameter: Decay Index n

TI is triggered by the force imbalance in the vertical direction (the upward “hoop” force versus the downward strapping force acting on the MFR) and is often quantified by the decay index n of the potential strapping field (Bateman 1978; Kliem & Török 2006):

$$n = -\frac{\partial \log(B_{\text{ext}})}{\partial \log(h)}, \quad (2)$$

where B_{ext} denotes the external strapping field at a geometrical height h above the surface. For each event, we first followed the procedures described by Sun et al. (2015) to identify the flaring polarity inversion line (FPIL) mask, which demarcates the AR core

⁴ $\langle \text{CWsin}\theta \rangle = \langle \sum_i |J_i| \theta_i \rangle / \langle \sum_i |J_i| \rangle$, where θ is the angle between \mathbf{B} and \mathbf{J} .

⁵ $|f_i| = |(\nabla \cdot \mathbf{B})_i| / (6|B_i|/\Delta x)$, where Δx is the grid spacing.

Table 1
Event List

No.	Flare SXR Peak Time, Class	NOAA AR	Position	Type ^a E/C	E_{CME}^b (10^{32} erg)	E_{free}^c (10^{32} erg)	h_{apex}^d (Mm)	d^e (Mm)	n^f	$ Z_w ^g$
1	SOL2011-02-13T17:38, M6.6	11158	S20E04	E	0.007	1.1 ± 0.4	5.4 ± 0.7	18.6 ± 2.0	0.58 ± 0.16	0.39 ± 0.03
2	SOL2011-02-15T01:56, X2.2	11158	S20W10	E	0.1	2.6 ± 1.0	13.1 ± 1.8	28.4 ± 2.0	0.86 ± 0.46	0.62 ± 0.04
3	SOL2011-03-09T23:23, X1.5	11166	N08W09	C	...	2.2 ± 0.9	12.8 ± 1.3	33.9 ± 1.4	0.62 ± 0.04	0.73 ± 0.21
4	SOL2011-07-30T02:09, M9.3	11261	S20W10	C	...	1.1 ± 0.4	7.1 ± 0.6	20.0 ± 0.6	0.45 ± 0.12	0.47 ± 0.14
5	SOL2011-08-03T13:48, M6.0	11261	N16W30	E	0.2	2.1 ± 0.8	18.1 ± 1.9	54.8 ± 1.3	1.28 ± 0.12	0.73 ± 0.16
6	SOL2011-09-06T01:50, M5.3	11283	N14W07	E	0.07	0.8 ± 0.3	10.7 ± 0.9	35.7 ± 2.5	0.86 ± 0.14	0.63 ± 0.09
7	SOL2011-09-06T22:20, X2.1	11283	N14W18	E	0.3	1.0 ± 0.4	22.2 ± 0.9	35.9 ± 7.4	0.98 ± 0.33	0.98 ± 0.20
8	SOL2011-10-02T00:50, M3.9	11305	N12W26	C	...	1.0 ± 0.4	7.6 ± 1.1	21.5 ± 5.0	0.63 ± 0.08	0.55 ± 0.09
9	SOL2012-01-23T03:59, M8.7	11402	N28W21	E	6.2	3.0 ± 1.2	19.4 ± 0.7	31.1 ± 0.9	0.79 ± 0.11	1.08 ± 0.20
10	SOL2012-03-07T00:24, X5.4	11429	N17E31	E	5.0	9.3 ± 3.6	14.4 ± 0.9	30.0 ± 2.0	0.89 ± 0.11	0.62 ± 0.06
11	SOL2012-03-09T03:53, M6.3	11429	N15W03	E	0.3	6.8 ± 2.7	10.6 ± 0.6	65.6 ± 8.7	0.78 ± 0.09	0.78 ± 0.15
12	SOL2012-07-02T10:52, M5.6	11515	S17E08	E	0.02	1.4 ± 0.5	12.6 ± 0.7	33.0 ± 3.7	0.60 ± 0.18	1.44 ± 0.16
13	SOL2012-07-12T16:49, X1.4	11520	S15W01	E	0.3	5.8 ± 2.3	9.3 ± 0.7	32.8 ± 0.8	0.51 ± 0.06	0.81 ± 0.09
14	SOL2013-04-11T07:16, M6.5	11719	N09E12	E	0.8	0.5 ± 0.2	13.5 ± 1.6	37.0 ± 3.1	0.61 ± 0.12	0.92 ± 0.17
15	SOL2013-10-24T00:30, M9.3	11877	S09E10	E	0.02	1.5 ± 0.6	8.3 ± 0.4	30.2 ± 7.4	0.18 ± 0.20	0.99 ± 0.12
16	SOL2013-11-01T19:53, M6.3	11884	S12E01	C	...	1.2 ± 0.5	8.3 ± 0.3	34.6 ± 1.7	0.70 ± 0.23	1.15 ± 0.21
17	SOL2013-11-03T05:22, M4.9	11884	S12W17	C	...	0.9 ± 0.4	8.8 ± 2.8	19.2 ± 7.2	0.53 ± 0.12	0.81 ± 0.14
18	SOL2013-11-05T22:12, X3.3	11890	S12E44	E	0.08	1.9 ± 0.7	7.7 ± 0.4	29.0 ± 0.5	0.31 ± 0.18	0.54 ± 0.14
19	SOL2013-11-08T04:26, X1.1	11890	S12E13	E	0.1	1.1 ± 0.4	8.3 ± 0.4	20.1 ± 2.9	0.28 ± 0.19	0.59 ± 0.08
20	SOL2014-01-07T18:32, X1.2	11944	S15W11	E	3.7	6.0 ± 2.3	19.9 ± 0.8	97.4 ± 1.1	0.61 ± 0.07	0.84 ± 0.15
21	SOL2014-02-02T09:31, M4.4	11967	S10E13	C	...	6.7 ± 2.6	7.8 ± 0.9	31.0 ± 1.3	0.43 ± 0.05	0.66 ± 0.09
22	SOL2014-02-04T04:00, M5.2	11967	S14W06	C	...	6.3 ± 2.5	8.0 ± 1.1	20.5 ± 5.4	0.67 ± 0.09	0.67 ± 0.11
23	SOL2014-03-29T17:48, X1.1	12017	N10W32	E	0.07	1.5 ± 0.6	7.9 ± 0.4	36.9 ± 3.4	0.73 ± 0.19	1.26 ± 0.09
24	SOL2014-04-18T13:03, M7.3	12036	S20W34	E	1.4	3.1 ± 1.2	25.8 ± 2.7	38.2 ± 3.3	1.07 ± 0.10	0.75 ± 0.12
25	SOL2014-09-10T17:45, X1.6	12158	N11E05	E	1.7	2.6 ± 1.0	8.2 ± 1.2	46.2 ± 2.5	0.42 ± 0.06	0.49 ± 0.09
26	SOL2014-10-22T14:28, X1.6	12192	S14E13	C	...	22.8 ± 8.9	5.5 ± 0.4	35.0 ± 1.0	0.22 ± 0.04	0.72 ± 0.03
27	SOL2014-10-24T21:41, X3.1	12192	S22W21	C	...	29.2 ± 11.4	23.8 ± 2.9	101.6 ± 12.7	0.70 ± 0.08	0.97 ± 0.26
28	SOL2014-11-07T17:26, X1.6	12205	N17E40	E	0.4	4.2 ± 1.6	7.7 ± 0.9	44.7 ± 0.8	0.66 ± 0.13	1.03 ± 0.11
29	SOL2014-12-04T18:25, M6.1	12222	S20W31	C	...	0.7 ± 0.3	12.9 ± 0.3	55.4 ± 1.1	0.56 ± 0.10	1.05 ± 0.17
30	SOL2014-12-17T04:51, M8.7	12242	S18E08	E	0.2	5.9 ± 2.3	27.5 ± 1.8	64.6 ± 0.6	1.34 ± 0.10	0.71 ± 0.12
31	SOL2014-12-18T21:58, M6.9	12241	S11E15	E	N/A ^h	2.2 ± 0.9	43.6 ± 0.4	36.9 ± 3.4	1.57 ± 0.10	1.08 ± 0.14
32	SOL2014-12-20T00:28, X1.8	12242	S19W29	E	0.8	11.8 ± 4.6	10.6 ± 0.4	41.7 ± 1.2	0.65 ± 0.06	0.91 ± 0.09
33	SOL2015-03-12T14:08, M4.2	12297	S15E06	C	...	2.9 ± 1.1	3.2 ± 0.3	25.0 ± 3.8	0.36 ± 0.15	0.54 ± 0.08
34	SOL2015-06-22T18:23, M6.5	12371	N13W06	E	0.3	6.9 ± 2.7	12.2 ± 1.8	44.2 ± 2.3	0.92 ± 0.06	1.14 ± 0.05
35	SOL2015-06-25T08:16, M7.9	12371	N12W40	E	4.1	6.9 ± 2.7	20.1 ± 0.6	42.2 ± 2.6	0.74 ± 0.20	0.93 ± 0.07
36	SOL2015-09-28T14:58, M7.6	12422	S20W28	C	...	1.7 ± 0.7	10.3 ± 0.2	42.7 ± 7.3	0.44 ± 0.13	0.74 ± 0.21
37	SOL2017-09-04T20:33, M5.5	12673	S10W11	E	N/A ⁱ	5.4 ± 2.1	2.4 ± 0.5	16.9 ± 1.5	0.80 ± 0.27	0.70 ± 0.08
38	SOL2017-09-06T12:02, X9.3	12673	S09W34	E	N/A ⁱ	1.3 ± 0.5	5.0 ± 0.5	18.5 ± 4.5	$0.6w3 \pm 0.09$	0.79 ± 0.14

Notes.^a Flare type: (E)jective or (C)onfined.^b CME Kinetic energy, from the *LASCO* CME catalog.^c Free magnetic energy with a 39% uncertainty (see Section 2).^d Apex height of MFRs with $\pm 1\sigma$ uncertainty obtained from NLFF field lines forming the MFRs.^e Footpoint distance of MFRs with $\pm 1\sigma$ uncertainty obtained from NLFF field lines forming the MFRs.^f Decay index with $\pm 1\sigma$ uncertainty calculated over the FPIL mask (see Section 3.1).^g Twist number with $\pm 1\sigma$ uncertainty calculated over the NLFF field lines forming the MFRs (see Section 3.2).^h Not available due to the data gap of *LASCO* C2.ⁱ Not available in the *LASCO* CME catalog.

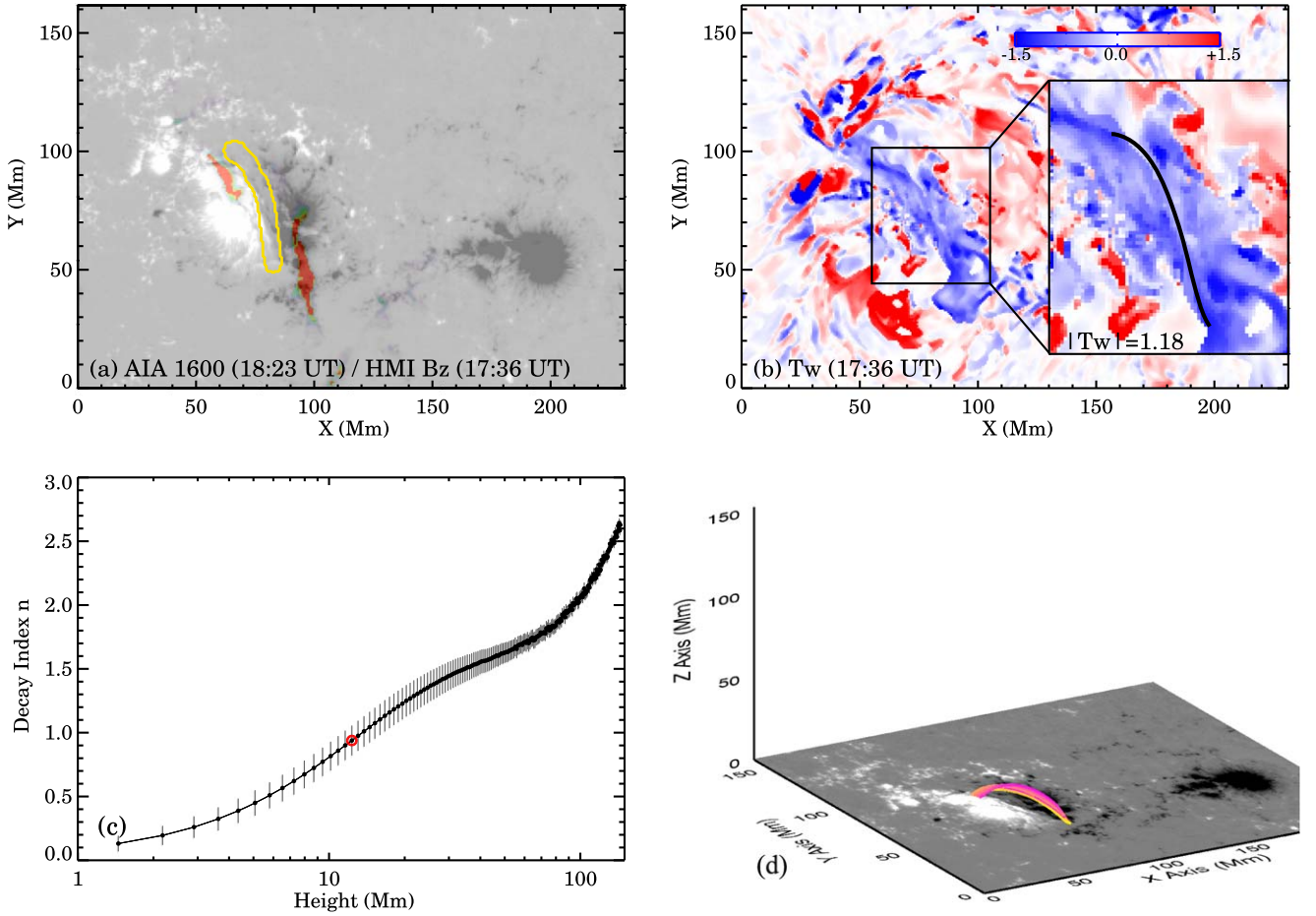


Figure 1. Magnetic field of the eruptive M6.5 flare (SOL2015-06-22T18:23) of AR 12371. (a) A blend of an AIA UV 1600 Å image at the flare peak time with the pre-flare HMI vector magnetogram B_z , superimposed with the yellow contours of the flaring polarity inversion line (FPIL) mask. Both AIA and HMI maps are de-rotated to a reference pre-flare time (17:36 UT in this case) and re-mapped with the CEA projection. (b) The twist number T_w map derived from the NLFF field, scaled between ∓ 1.5 (blue/red). The rectangle enclosing the flaring core region is zoomed in and displayed in the inset. The superimposed black line shows a representative field line of the MFR, whose $|T_w|$ is annotated. (c) The height profile of decay index n above the FPIL region derived from the potential field model. The error bars indicate a $\pm 1\sigma$ spread, evaluated from 908 profiles in the FPIL region in this case. The red circle marks the data point at h_{apex} . (d) A 3D perspective of the MFR extrapolated from the NLFF field.

field where the MFR resides and the instability initiates. The HMI B_z map together with the UV 1600 Å image taken near the flare peak time by the Atmospheric Imaging Assembly (AIA; Lemen et al. 2012) on board *SDO* was used in this step. Figures 1(a) and 2(a) show the composite image of both B_z and AIA 1600 Å maps of the ejective M6.5 (confined M4.2) flare, superimposed with the yellow contour of the FPIL mask. The horizontal component of the potential field directly above the FPIL is used to approximate the strapping magnetic field. Figures 1(c) and 2(c) show the corresponding profile of n (averaged over all FPIL mask pixels) as a function of height h . The mean value of n at the MFR's apex height h_{apex} with the $\pm 1\sigma$ uncertainty calculated over the FPIL mask is listed in Table 1.

3.2. KI Parameter: Twist Number T_w

In our NLFF field models, the twist number T_w (Berger & Prior 2006) is computed as

$$\begin{aligned} T_w &= \int_L \frac{\mu_0 \mathbf{J} \cdot \mathbf{B} / |\mathbf{B}|}{4\pi |\mathbf{B}|} dl \\ &= \int_L \frac{\nabla \times \mathbf{B} \cdot \mathbf{B}}{4\pi |\mathbf{B}|^2} dl = \frac{1}{4\pi} \int_L \alpha dl, \end{aligned} \quad (3)$$

where α is the force-free parameter and $\frac{\nabla \times \mathbf{B} \cdot \mathbf{B}}{4\pi |\mathbf{B}|^2}$ is thought of as a local density of twist along each individual field line. T_w is a good approximation of the traditional physical concept of twist Φ (i.e., winding of magnetic field lines around an axis) in the vicinity of the axis of a nearly cylindrically symmetric MFR (Liu et al. 2016). While the computation of Φ requires the correct determination of the axis, T_w can be computed straightforwardly for any field lines without restoring the geometry of an MFR, and thus providing a convenient means to quantify KI in practice. To calculate T_w we used the code developed by Liu et al. (2016), which is available online.⁶

We applied the code to the extrapolated 3D NLFF field to produce the T_w map in which each pixel is assigned by the T_w value of the NLFF field line threading from this pixel. Figures 1(b) and 2(b) show the T_w map of the ejective M6.5 (confined M4.2) flare of AR 12371 (AR 12297). Near the two ends of the FPIL region, we see two conjugate regions with enhanced T_w of the same sign, which are considered to host the footpoints of the MFR. The mean unsigned twist number $|T_w|$ of the NLFF field lines forming the MFR (derived from NLFF field; see the bottom panels of Figures 1 and 2) and its $\pm 1\sigma$ uncertainty are listed in Table 1.

⁶ <http://staff.ustc.edu.cn/~rliu/qfactor.html>

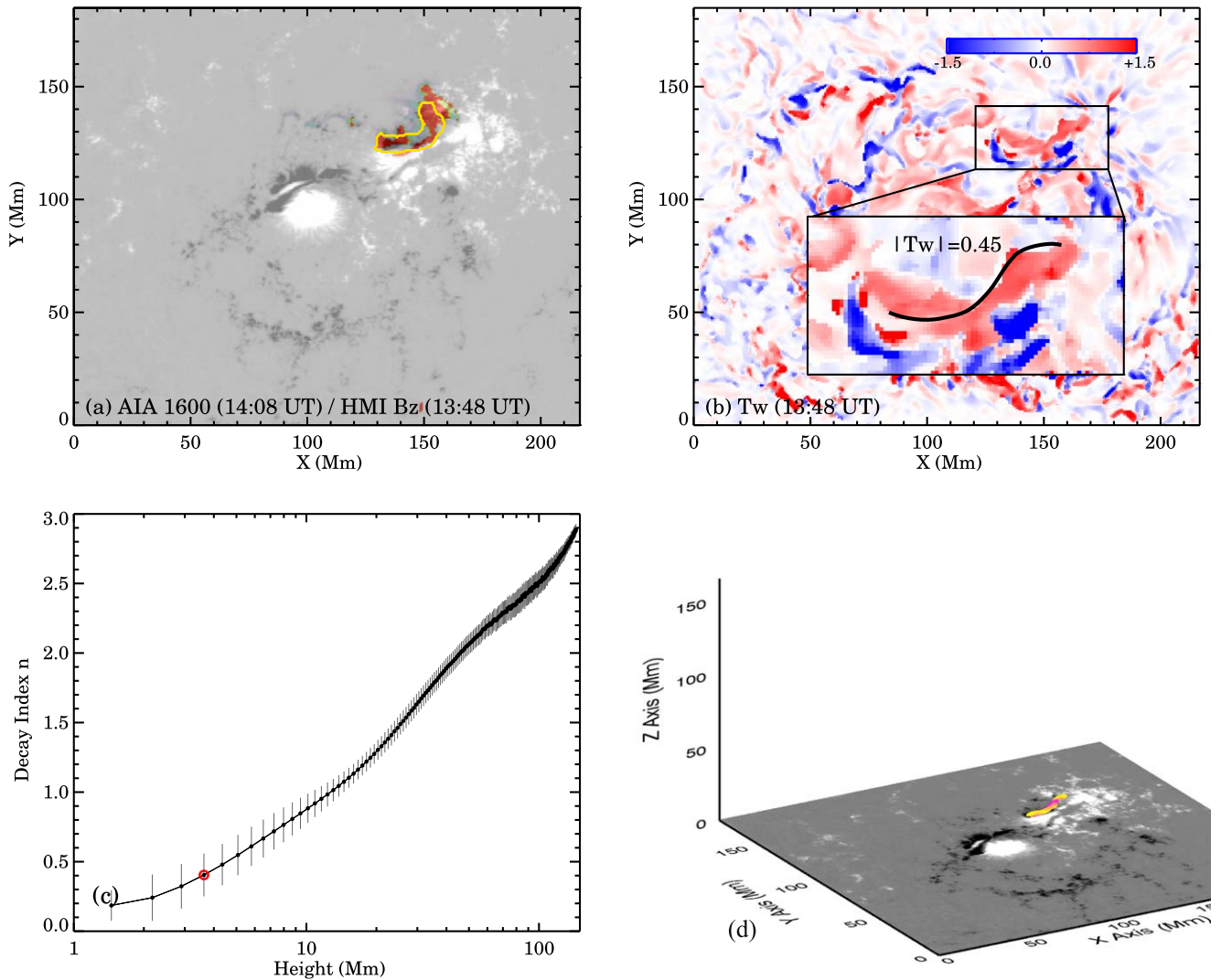


Figure 2. Magnetic field of the confined M4.2 flare (SOL2015-03-12T14:08) of AR 12297. Same layout as Figure 1.

4. Results

Figure 3 shows the scatter diagram of TI parameters n versus KI parameters T_w for the 38 flares. The black symbols represent the confined flares and the rest, ejective flares. For ejective flares, the color is assigned according to the associated CME’s kinetic energy. At a glance, our result does not clearly show the four distinct eruption regimes found by the laboratory experiment (Figure 2 of Myers et al. 2015). It is partly due to the fact that the confined and ejective flares are not clearly distinguished in terms of T_w . Instead, we see the clustering of the confined CME-less flares in the lower part of the diagram ($0.2 \lesssim n \lesssim 0.7$), while the ejective flares spread out over most of the n range ($0.2 \lesssim n \lesssim 1.6$). Note that the 12 flares with $n \gtrsim 0.8$ are all ejective, in which case we can regard this as a sufficient condition for CME. However, not all flares of $n \lesssim 0.8$ are confined. Only 12 out of the 26 flares with $n \gtrsim 0.8$ are confined and the other 14 flares are ejective. Thus, the criterion, $n > n_{\text{crit}} \simeq 0.8$ found here is not a necessary condition for a CME. Note also that this value of $n_{\text{crit}} \simeq 0.8$ found here is much lower than those typically cited in other solar studies ($n_{\text{crit}} \simeq 1.1\text{--}1.3$ in Démoulin & Aulanier 2010, for

instance), although it agrees well with the critical decay index found in the laboratory experiment performed by Myers et al. (2015). We presume that the difference arises from the fact that the decay indices were often evaluated for large loops (typically in the height range of 42–105 Mm) in the previous solar studies, whereas the MFRs with lower heights are included in the present statistical study.

Based on the experimentally measured TI versus KI parameter diagram, Myers et al. (2015) report a previously unknown instability regime—failed torus. The “failed torus” events occur when the guide magnetic field interacts with electric currents in the MFR to produce a dynamic tension force that brakes the ascension in the torus-unstable region. Our limited samples, however, do not show the presence of this regime. Instead, all the MFRs that exceeded a certain torus threshold, ~ 0.7 in our cases, are developing into CMEs. Presumably, the dynamic tension force in the solar cases is too weak to halt eruptions.

The top panels of Figure 4 show the histograms of $|T_w|$, n , and E_{free} for both ejective and confined flares. To investigate the MFR geometry as a possible factor for the eruptiveness, we also compared the histograms of h_{apex} , distance d between the

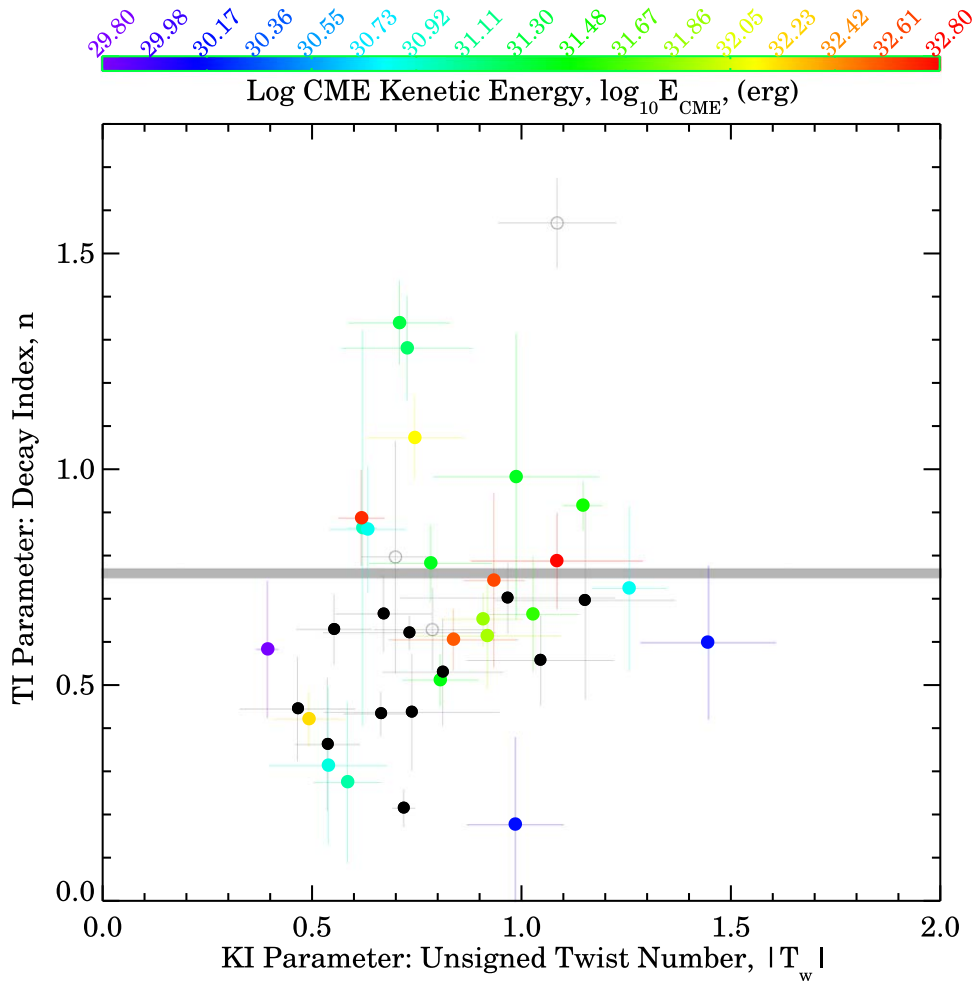


Figure 3. Scatter diagram of TI parameter n vs. KI parameter $|T_w|$. Black and colored symbols correspond to the confined and ejective flares, respectively. For ejective flares, the color is assigned according to the associated CME’s kinetic energy, indicated by the color code. Three uncolored open symbols represent the three ejective flares in the absence of E_{CME} information. The error bars indicate a $\pm 1\sigma$ spread. The horizontal gray line is drawn to illustrate $n_{\text{crit}} \simeq 0.8$.

MFR footpoints, and h_{apex}/d for ejective and confined flares in the bottom panels of Figure 4. For a quantitative comparison between the ejective and confined samples, we performed the Student’s t -test to determine the t -statistic (t ; a ratio of the difference between two groups to the difference within the groups) and its significance (α ; the probability that the results occurred by random chance) for each of the parameters. Briefly speaking, the larger the t -statistic, the greater the difference there is between the two groups. The lower the significance, the more confidently one can replicate the results. As one might expect, the most appreciable segregation between the two groups is in the histograms of n with $t = 2.337$ and $\alpha = 0.025$. That is, the null hypothesis (i.e., there is no difference in mean n between the ejective and confined flares) can be rejected at the $100(1 - \alpha)\% = 97.5\%$ level of confidence. By comparison, the role of T_w in distinguishing between ejective and confined groups is questionable ($t = 0.995$ and $\alpha = 0.32$). Based on this result, we conclude that the TI rather than the KI plays a more important role in differentiating between the ejective and the confined flares.

To illustrate the relationship between the MFR geometry and the strapping effect, Figure 5 shows the scatter diagrams of (a) h_{apex} versus d , (b) n versus d , (c) n versus h_{apex} , and (d) n versus h_{apex}/d . The linear Pearson correlation coefficient (CC) and the probability of obtaining a certain CC by chance (P_{CC}) are given in the each

panel. We see a moderate positive linear correlation between h_{apex} and d with a CC of 0.62 (Figure 5(a)). The linear fit to these two data pairs is $h_{\text{apex}} = 2.65 + 0.26 \times d$, suggesting that MFRs in our solar cases are of a more flat-arched structure or are only a minor segment of a circular structure. A strong positive correlation between n and h_{apex} with a CC of 0.76 is shown in Figure 5(c). This should not be surprising, as the strapping magnetic field decays with height so that a low-lying/high-lying MFR is usually relevant to a stronger/weaker strapping effect.

5. Discussion and Conclusion

The previous laboratory experiment reveals that the eruptiveness of MFRs is dependant on the interplay between the TI and KI, as represented by the n - T_w diagram. In this paper, we intended to establish a solar counterpart to the diagram, by which we may be able to tell the likelihood of a CME based on the observed n and T_w parameters. The key results are summarized and discussed as follows.

First, the TI quantified by n appears to play an important role in differentiating between ejective and confined flares. However, the TI onset criteria ($n \geq n_{\text{crit}} = \sim 0.75$) found here is not a necessary condition for CMEs. Some MFRs in the TI-stable regime still manage to break through the strong strapping field and evolve into CMEs. It therefore implies that an additional

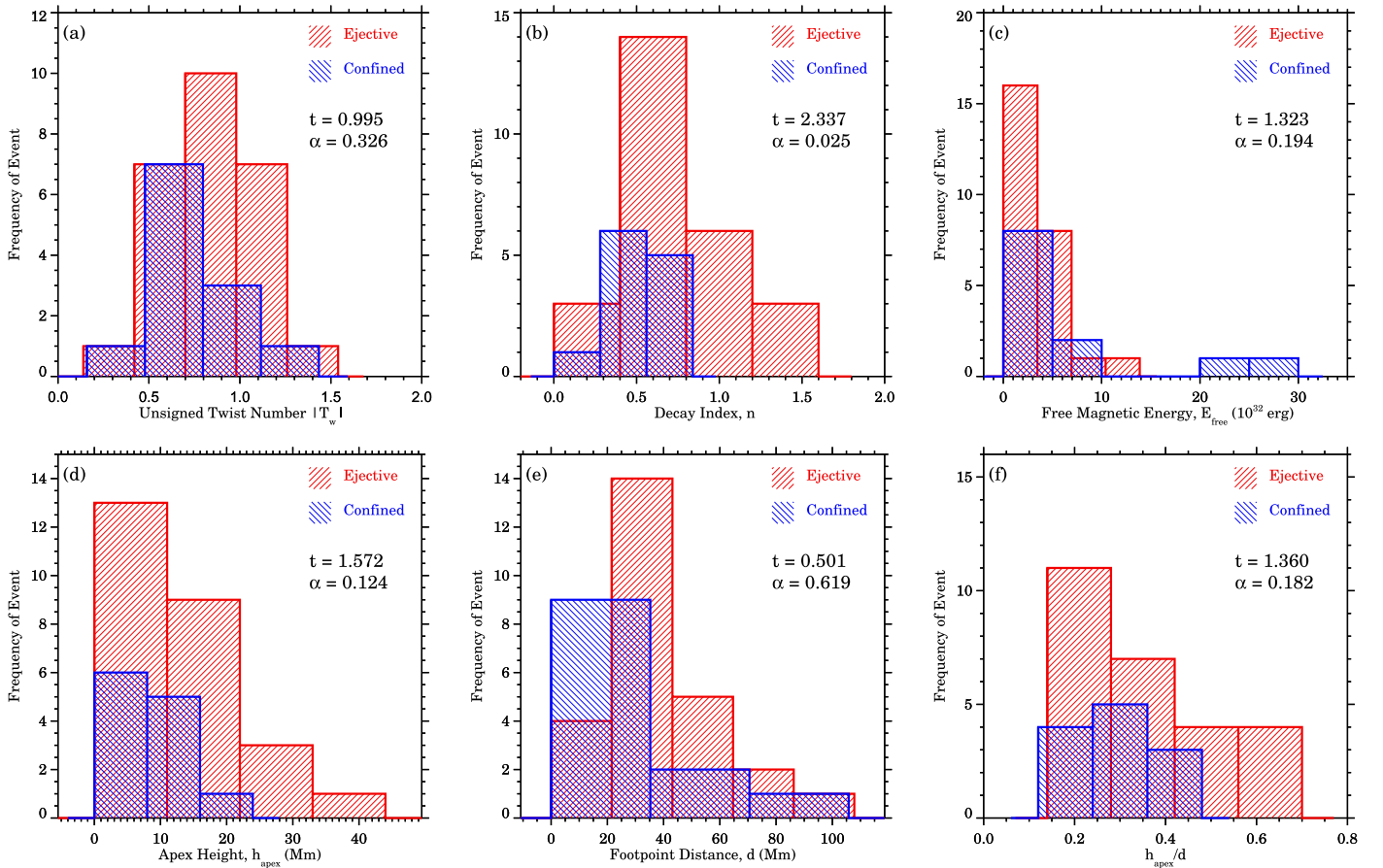


Figure 4. Histograms of (a) $|T_w|$, (b) n , (c) E_{free} , (d) h_{apex} , (e) d , and (f) h_{apex}/d . Red/Blue represents ejective/confined flares. Student's t -statistic (t) and its significance (α) are shown in each panel.

trigger and driving mechanism may be involved in solar eruptions. A very likely candidate for the alternative process is magnetic reconnection during solar flares. Actually, there are a number of analytical/numerical models invoking magnetic reconnection in the mechanism of CMEs. For instance, in the magnetic breakout model (Antiochos et al. 1999), magnetic reconnection leads to the progressive transformation of the magnetic configuration, allowing an MFR to burst open. In the tether-cutting reconnection model (Moore et al. 2001), magnetic reconnection below an MFR “cuts” the “tethers” of the strapping field to unleash CMEs. Such non-ideal MHD processes are absent in the laboratory experiment, which was designed to simulate eruptions solely in terms of an ideal MHD process.

Second, it is unclear in this study whether the KI represented by T_w is a major factor for solar eruption. Two MFRs with the highest value of $T_w > 1.2$ erupted, but many other MFRs with smaller values of T_w were also able to erupt, and we tend to believe that KI is less influential. We consider two possible caveats. The first concerns the ongoing debate whether a helical magnetic structure pre-exists before an eruption (Chen 1989; Low 1994; Fan & Gibson 2004) or is formed in the course of an eruption via magnetic reconnection (van Ballegoijen & Martens 1989; Amari et al. 2000; MacNeice et al. 2004). There is observational evidence in favor of each scenario (e.g., Dere et al. 1999; Qiu et al. 2007; Liu et al. 2010b; Song et al. 2014; Wang et al. 2015; Yan et al. 2015; Gopalswamy et al. 2017). In the latter case, it is not surprising that T_w derived from the pre-eruption magnetic field may be underestimated and cannot

correctly predict the eruptiveness. The second possibility is that helical KI could result in the deformation of a MFR, but may not allow a huge expansion of the MFR to produce a CME (Green et al. 2018). In this sense, we may consider that KI might be capable of initiating a filament eruption and a flare, but may not be the key factor in driving a CME into the heliosphere.

Third, the laboratory experiment by Myers et al. (2015) shows that there can be both failed TI and failed KI events. Namely, MFRs have greater difficulty in eruption than the solar community believed. This is contrary to our results that even the TI-stable ($n < 0.75$) ones can erupt and CMEs can occur regardless of the KI parameter T_w . As mentioned earlier, we speculate that magnetic reconnection, which was absent in the laboratory experiment, may be the factor causing the differences between the laboratory and the present solar observations, if it alleviates the difficulties in eruption.

The differences between the laboratory results and our results may also arise from multiple sources of assumptions and approximations of this study in contrast to the lab experiment. In the present study, the TI and KI parameters n and T_w are not directly measured in observations, but rather estimated from MFRs in NLFF field models. The identification of MFRs relies on the quality of NLFF field extrapolation. Although the up-to-date NLFF field extrapolation technique employed here was evaluated thoroughly in comparison with a 3D radiative MHD model and was found to offer a reasonably high accuracy of the coronal field reconstruction (Wiegelmann & Inhester 2010; Wiegelmann et al. 2010; Fleishman et al. 2017), the direct

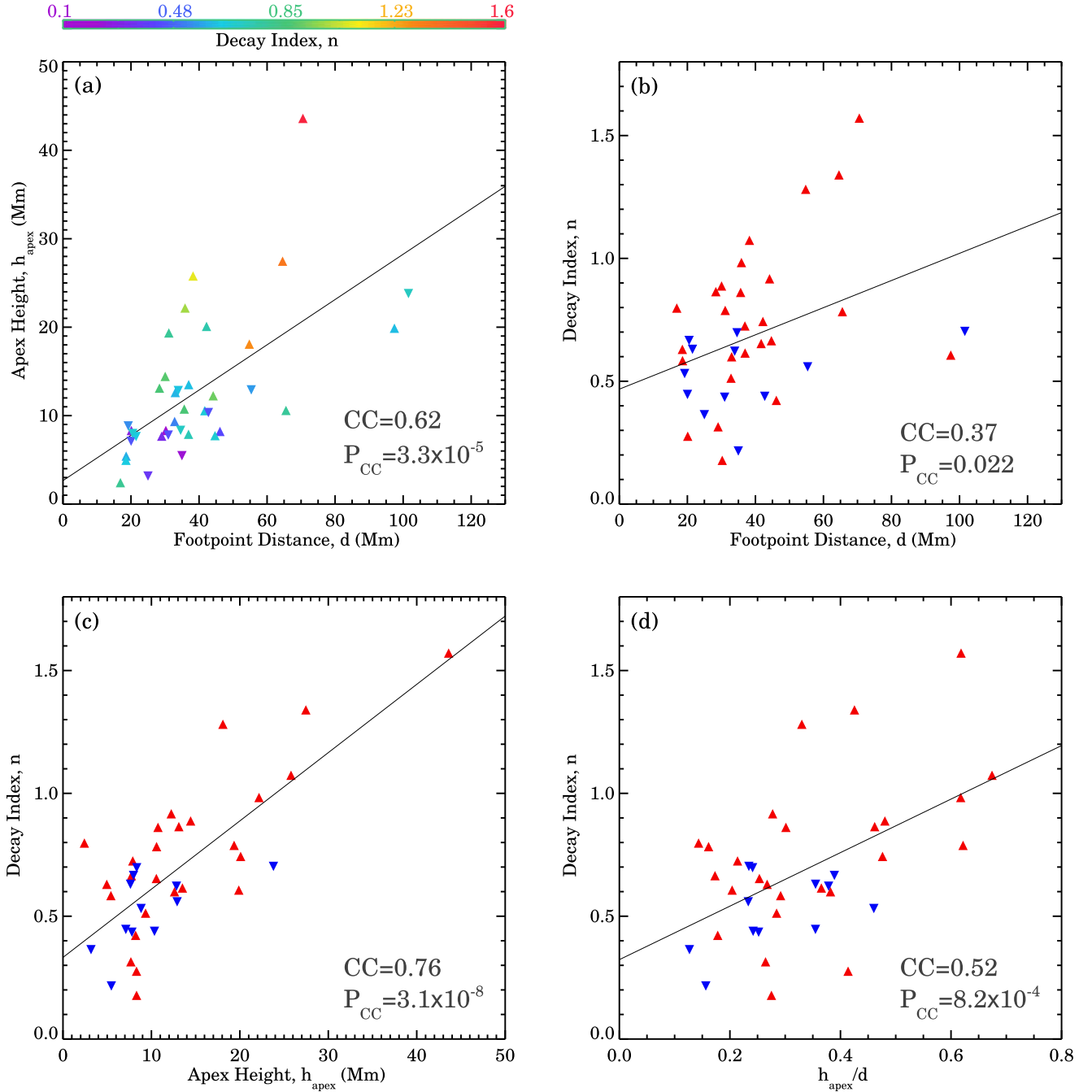


Figure 5. Scatter diagrams of (a) apex height h_{apex} vs. footpoint distance d of MFRs, (b) n vs. d , (c) n vs. h_{apex} , and (d) n vs. h_{apex}/d . Triangles and upside-down triangles represent ejective and confined flares, respectively. The color is assigned either according to the value of n (a) indicated by the color code, or red/blue for ejective/confined flares ((b)–(c)). The linear Pearson correlation coefficient (CC) and the probability of obtaining a certain CC by chance (P_{CC}) are shown in each panel. The solid lines denote the least-squares fits to data pairs, which are $h_{\text{apex}} = 2.65 + 0.26 \times d$, $n = 0.47 + 0.0055 \times d$, $n = 0.33 + 0.028 \times h_{\text{apex}}$, and $n = 0.32 + 1.09 \times h_{\text{apex}}/d$.

validation of NLFF fields still cannot be performed due to the lack of the coronal magnetic field diagnostics. We would like to caution that NLFF field extrapolation has intrinsic limitations associated with the force-free assumption and is subject to numerous uncertainties in the data reduction and modeling process that are not reflected in our results. It may be that n and/or T_w could not be accurately calculated under the observational limits. In addition, the KI parameter T_w is derived from and averaged over individual field lines, assuming that it is related to the winding of field lines around the axis, but

actually the twist of an MFR could be underestimated by its built-in assumption.

Finally, we would like to mention that the present statistical study is a step forward in accessing the role of the TI and KI in solar eruptions. Detailed studies of the pre-to-post-flare magnetic configuration are also needed to better understand the underlying physics, which will be conducted in the future.

We thank the anonymous referee for constructive comments. We thank the NASA *SDO* team for HMI and AIA data. HMI and

AIA are instruments on board *SDO*, a mission for NASA's Living with a Star program. We thank CDAW Data Center at Goddard Space Flight Center for providing the CME catalog, which is supported by NASA's Living with a Star program and the *SOHO* project. We thank Dr. Rui Liu for developing the code to calculate the twist number. J.J., N.L., Y.X., C.L., and H.W. were supported by NASA grants NNX16AF72G, 80NSSC17K0016 (Grand Challenge) and 80NSSC18K0673 (GI), NSF grants AGS 1408703, and 1539791. J.L. was supported by the BK21 plus program through the National Research Foundation (NRF) funded by the Ministry of Education of Korea to Kyung Hee University.

ORCID iDs

Ju Jing  <https://orcid.org/0000-0002-8179-3625>
 Hantao Ji  <https://orcid.org/0000-0001-9600-9963>
 Haimin Wang  <https://orcid.org/0000-0002-5233-565X>

References

- Alissandrakis, C. E. 1981, *A&A*, **100**, 197
 Amari, T., Luciani, J. F., Mikic, Z., & Linker, J. 2000, *ApJL*, **529**, L49
 Antiochos, S. K., DeVore, C. R., & Klimchuk, J. A. 1999, *ApJ*, **510**, 485
 Aulanier, G., Török, T., Démoulin, P., & DeLuca, E. E. 2010, *ApJ*, **708**, 314
 Bateman, G. 1978, *MHD Instabilities* (Cambridge, MA: MIT Press)
 Baty, H. 2001, *A&A*, **367**, 321
 Baumgartner, C., Thalmann, J. K., & Veronig, A. M. 2018, *ApJ*, **853**, 105
 Berger, M. A., & Prior, C. 2006, *JPhA*, **39**, 8321
 Chen, J. 1989, *ApJ*, **338**, 453
 Cui, Y., Wang, H., Xu, Y., & Liu, S. 2018, *JGRA*, **123**, 1704
 De Rosa, M. L., Schrijver, C. J., Barnes, G., et al. 2009, *ApJ*, **696**, 1780
 Démoulin, P., & Aulanier, G. 2010, *ApJ*, **718**, 1388
 Dere, K. P., Brueckner, G. E., Howard, R. A., Michels, D. J., & Delaboudiniere, J. P. 1999, *ApJ*, **516**, 465
 Falconer, D. A., Moore, R. L., & Gary, G. A. 2006, *ApJ*, **644**, 1258
 Falconer, D. A., Moore, R. L., Gary, G. A., & Adams, M. 2009, *ApJL*, **700**, L166
 Fan, Y. 2010, *ApJ*, **719**, 728
 Fan, Y., & Gibson, S. E. 2003, *ApJL*, **589**, L105
 Fan, Y., & Gibson, S. E. 2004, *ApJ*, **609**, 1123
 Fan, Y., & Gibson, S. E. 2007, *ApJ*, **668**, 1232
 Fleishman, G. D., Anfinogentov, S., Loukitcheva, M., Mysh'yakov, I., & Stupishin, A. 2017, *ApJ*, **839**, 30
 Gopalswamy, N., Yashiro, S., Akiyama, S., & Xie, H. 2017, *SoPh*, **292**, 65
 Gopalswamy, N., Yashiro, S., Michalek, G., et al. 2009, *EM&P*, **104**, 295
 Green, L. M., Török, T., Vršnak, B., Manchester, W., & Veronig, A. 2018, *SSRv*, **214**, 46
 Guo, Y., Ding, M. D., Schmieder, B., et al. 2010, *ApJL*, **725**, L38
 Hood, A. W., & Priest, E. R. 1981, *GApFD*, **17**, 297
 Jing, J., Xu, Y., Lee, J., et al. 2015, *RAA*, **15**, 1537
 Kliem, B., & Török, T. 2006, *PhRvL*, **96**, 255002
 Lee, J., Liu, C., Jing, J., & Chae, J. 2016, *ApJL*, **831**, L18
 Lemen, J. R., Title, A. M., Akin, D. J., et al. 2012, *SoPh*, **275**, 17
 Liu, C., Lee, J., Jing, J., et al. 2010a, *ApJL*, **721**, L193
 Liu, R., Kliem, B., Titov, V. S., et al. 2016, *ApJ*, **818**, 148
 Liu, R., Liu, C., Wang, S., Deng, N., & Wang, H. 2010b, *ApJL*, **725**, L84
 Liu, Y. 2008, *ApJL*, **679**, L151
 Low, B. C. 1994, *PhPI*, **1**, 1684
 Low, B. C., & Lou, Y. Q. 1990, *ApJ*, **352**, 343
 MacNeice, P., Antiochos, S. K., Phillips, A., et al. 2004, *ApJ*, **614**, 1028
 Moore, R. L., Sterling, A. C., Hudson, H. S., & Lemen, J. R. 2001, *ApJ*, **552**, 833
 Myers, C. E., Yamada, M., Ji, H., et al. 2015, *Natur*, **528**, 526
 Nindos, A., & Andrews, M. D. 2004, *ApJL*, **616**, L175
 Nindos, A., Patsourakos, S., & Wiegmann, T. 2012, *ApJL*, **748**, L6
 Olmedo, O., & Zhang, J. 2010, *ApJ*, **718**, 433
 Qiu, J., Hu, Q., Howard, T. A., & Yurchyshyn, V. B. 2007, *ApJ*, **659**, 758
 Schou, J., Borrero, J. M., Norton, A. A., et al. 2012, *SoPh*, **275**, 327
 Song, H. Q., Zhang, J., Chen, Y., & Cheng, X. 2014, *ApJL*, **792**, L40
 Sun, X. 2013, arXiv:1309.2392
 Sun, X., Bobra, M. G., Hoeksema, J. T., et al. 2015, *ApJL*, **804**, L28
 Toriumi, S., Schrijver, C. J., Harra, L. K., Hudson, H., & Nagashima, K. 2017, *ApJ*, **834**, 56
 Török, T., & Kliem, B. 2003, *A&A*, **406**, 1043
 Török, T., & Kliem, B. 2005, *ApJL*, **630**, L97
 Török, T., & Kliem, B. 2007, *AN*, **328**, 743
 Török, T., Kliem, B., & Titov, V. S. 2004, *A&A*, **413**, L27
 Tziotziou, K., Georgoulis, M. K., & Raouafi, N.-E. 2012, *ApJL*, **759**, L4
 van Ballegooijen, A. A., & Martens, P. C. H. 1989, *ApJ*, **343**, 971
 Vourlidas, A., Howard, R. A., Esfandiari, E., et al. 2010, *ApJ*, **722**, 1522
 Wang, H., Cao, W., Liu, C., et al. 2015, *NatCo*, **6**, 7008
 Wheatland, M. S., Sturrock, P. A., & Roumeliotis, G. 2000, *ApJ*, **540**, 1150
 Wiegmann, T. 2004, *SoPh*, **219**, 87
 Wiegmann, T., & Inhester, B. 2010, *A&A*, **516**, A107
 Wiegmann, T., Inhester, B., & Sakurai, T. 2006, *SoPh*, **233**, 215
 Wiegmann, T., Thalmann, J. K., Inhester, B., et al. 2012, *SoPh*, **281**, 37
 Wiegmann, T., Yelles Chaouche, L., Solanki, S. K., & Lagg, A. 2010, *A&A*, **511**, A4
 Xu, Y., Liu, C., Jing, J., & Wang, H. 2012, *ApJ*, **761**, 52
 Yan, X. L., Xue, Z. K., Pan, G. M., et al. 2015, *ApJS*, **219**, 17
 Zuccarello, F. P., Aulanier, G., & Gilchrist, S. A. 2015, *ApJ*, **814**, 126